



Mathematical models for the effect of anti-vascular endothelial growth factor on visual acuity

David A. Edwards¹ · Brooks Emerick² · Anna Georgieva Kondic³ ·
Kristian Kiradjiev⁴ · Christopher Raymond¹ · Maxim Zyskin⁵

Received: 15 January 2020 / Revised: 9 June 2020 / Accepted: 13 September 2020 /

Published online: 24 September 2020

© Springer-Verlag GmbH Germany, part of Springer Nature 2020

Abstract

The standard of care treatment for neovascular age-related macular degeneration, delivered as ocular injection, is based on anti-vascular endothelial growth factor (anti-VEGF). The course of treatment may need to be modified quickly for certain patients based on their response. Models that track both the concentration and the response to an anti-VEGF treatment are presented. The specific focus is to assess the existence of analytical solutions for the different types of models. Both an ODE-based model and a map-based model illustrate the dependence of the solution on various biological parameters and allow the measurement of patient-specific parameters from experimental data. A PDE-based model incorporates diffusive effects. The results are consistent with observed values, and could provide a framework for practitioners to understand the effect of the therapy on the progression of the disease in both responsive and non-responsive patients.

Keywords Pharmacokinetics · Pharmacodynamics · Analytical solutions · Macular degeneration · Diffusion equation · Discrete modeling

Mathematics Subject Classification 35Q92 · 37N25 · 92C45 · 92C50

✉ David A. Edwards
dedwards@udel.edu

¹ Department of Mathematical Sciences, University of Delaware, Newark, DE 19716, USA

² Department of Mathematics, Kutztown University, Kutztown, PA 19530, USA

³ Certara, Princeton, NJ 08540, USA

⁴ Mathematical Institute, University of Oxford, Oxford OX2 6GG, UK

⁵ Department of Engineering Science, University of Oxford, Oxford OX1 3PJ, UK

1 Introduction

Age-related macular degeneration is a leading cause of blindness. In the neovascular variety (nAMD), abnormal blood vessels leak fluid into the sub-retinal space (see Fig. 1). This causes an increase in the central sub-field (retinal) thickness (CSFT), resulting in vision loss. CSFT is assessed via the use of optical coherence tomography (OCT), a non-invasive imaging test that uses light waves to take cross-sectional pictures of the retina. Drugs targeting vascular endothelial growth factor (VEGF) are delivered as injections in the vitreous chamber of the eye at regular intervals to stem this leakage (Wykoff et al. 2018). The introduction of these anti-VEGF drugs has revolutionized the treatment of nAMD. Despite this significant progress, gaps and challenges persist in the diagnosis of nAMD, initiation of treatment, and management of frequent intravitreal injections. To this day, nAMD remains a leading cause of blindness in the United States.

Controlled clinical trials typically take two years to complete. Questions and complexities remain when one wants to project the disease progression of an individual patient over a longer time period and under a real-world treatment paradigm. To elucidate these complexities, long-term extrapolation is needed. Mathematical modeling lends itself naturally to this task. Multiple efforts exist in the literature (e.g., Martínez-Cañada et al. 2016; McHugh et al. 2019; Roberts et al. 2016). Some consider the detailed pharmacokinetics (drug distribution, Awwad et al. 2015; Edington et al. 2017)

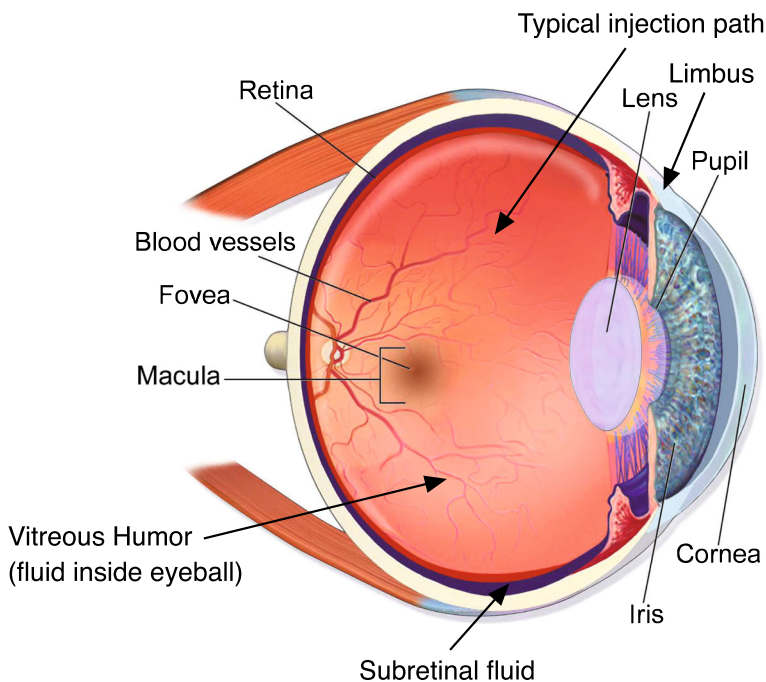


Fig. 1 Schematic of the eye. Adapted from Blausencom staff (2014)

and pharmacodynamics (how the drug impacts the biological system, Semeraro et al. 2015) in general and of specific molecules (e.g., Mulyukov et al. 2018). Others look at a more detailed representation of the eye, focusing on the delivery of the drug (e.g., del Amo et al. 2017; Kotha and Murtomäki 2014). Other authors consider the effects of the drug on patient outcomes. In particular, some models consider the drug's effect on various biological pathways (Hoyle and Aslam 2017), or how the drug impacts acuity loss (Mulyukov et al. 2018).

The mathematical representation also varies from compartment-based ODE approaches (both deterministic and stochastic) to computational methods with PDEs (mostly using finite element approaches). For example, Hoyle and Aslam (2017) create a generative model of nAMD, though that is purely based on simulations. In their elegant works, Hutton-Smith et al. (2016, 2017) use compartment-based ODE models that divide the eye into vitreous, aqueous, and retinal regions, accounting for transport between them and linking the drug (ranibizumab) concentration to the dynamics of the VEGF pathway only and not to a clinical outcome. In a detailed PK model, Zhang et al. (2018) use numerical simulations of PDEs to track the concentration in various portions of the eye but do not link the results to patient outcomes. In what follows, we build upon these efforts with the goal of investigating the existence of analytical solutions.

CSFT (as mentioned above), as well as the best-corrected visual acuity (BCVA) score, which is essentially the score determined from having the patient read an eye chart (Mulyukov et al. 2018), are commonly used to evaluate nAMD patients. As the treatment regimen progresses, the information from these two types of measurements (and others not considered here) should be able to guide the treating physician on the progress made by the patient. In a responsive subject, one would expect to see BCVA increase while CSFT decreases. Since the concentration \tilde{C} of the anti-VEGF decays over time as it is cleared by the body, this necessitates repeat treatment. Despite advances in delivery, ocular injections remain invasive. Therefore, it is desired that an individualized optimal regimen be created for each patient based on their disease history and response to therapy.

One would hope that there would be a direct relationship between the concentration \tilde{C} of the anti-VEGF treatment and these measurements. However, with time the body develops a tolerance for the medication, necessitating higher dosages to achieve the same result. Such effects are highly variable among patients, and hence so is the patient's response to medication. In this study, we gauge this variability by examining a small but representative sample of clinical data where patients were receiving some sort of anti-VEGF therapy. None of the patient-specific characteristics were shared, so we had no information about their age, gender, co-morbidities or co-medications. Hence we are blinded to the patient-specific journey. Instead, we aim to achieve two main goals. First, we seek to establish parameter values unique to our mathematical models that describe patient-specific response. Second, we investigate the existence of analytical solutions. Answers to these two questions provide feasibility assessment for the development of a fast and fully-predictive tool.

In this work, we largely focus on the BCVA score; discussion of the specifics of CSFT is presented in the final section. In Sect. 2, we derive and solve a three-dimensional ODE system which provides estimates for how the score changes with

time in the presence of a treatment regimen, and fit the model to actual patient data. In Sect. 3, we derive an analogous discrete model, and again fit it to actual patient data. In Sect. 4, we present a spatial model to consider the diffusion aspects of the medication, at least in an idealized geometry, and fit to the patient data. Despite the limitations mentioned for each of these modeling approaches, they constitute a foundation for how one can predict long-term behavior based upon short-term results, incorporate patient-specific characteristics, and investigate the efficacy of different dosing frequencies. In Sect. 5, we conclude with a discussion of our results and suggestions for future work.

2 An ODE model

2.1 Governing equations

We begin by considering a continuous ODE model for the response of the measurements to the treatment regimen, as motivated by Mulyukov et al. (2018). Though more complicated multicompartment ODE models for the concentration \tilde{C} exist (Hutton-Smith et al. 2016, 2017), our focus here is different: namely to predict patient outcomes through the BCVA measurement \tilde{a} , preferably through analytic solutions that can easily be implemented in an app. As will be shown, our model does provide good results for the acuity, and hence even a simple one-component PK model can capture the essential features of the system. Of course, an ODE model for the concentration does not address diffusive transport in the eye; that shortcoming will be remedied in Sect. 4.

During the treatment regime, dosages of mass \tilde{D} are administered at time $\tilde{t} = 0$ and N subsequent times \tilde{t}_i . These values can be converted to a mass concentration (the preferred measurement) by dividing by the apparent volume V of the vitreous fluid in the eye. (Parameter values may be found in the Appendix.)

As time passes, the amount of medication in the vitreous chamber of the eye will decrease, either through transport to the aqueous region in the front of the eye, or transport via the episcleral vein at the back of the eye (Zhang et al. 2018). Following Hutton-Smith et al. (2017), we model this process as exponential decay with elimination constant k_C . Hence the full governing equation for the concentration becomes

$$\frac{d\tilde{C}}{d\tilde{t}} = -k_C \tilde{C} + \frac{\tilde{D}}{V} \sum_{i=0}^N \delta(\tilde{t} - \tilde{t}_i), \quad \tilde{C}(0) = 0, \quad \tilde{t}_0 = 0. \quad (1)$$

In the absence of medication, we assume that the BCVA measurement $\tilde{a}(\tilde{t})$ of a patient with nAMD decays exponentially at a rate \tilde{k}_{out} to a nonzero value which is consistent with blindness. This decay is then balanced by an “inflow” of acuity, which the medication is designed to enhance. The resulting equation is

$$\frac{d\tilde{a}}{d\tilde{t}} = \tilde{k}_{\text{in}}[1 + E(\tilde{C})] - \tilde{k}_{\text{out}}\tilde{a}, \quad \tilde{a}(0) = \tilde{a}_0. \quad (2)$$

Here the function $E(\tilde{C})$ is the *effectiveness* of the medication, and \tilde{k}_{in} represents some natural “inflow” of acuity which balances this decay: hence $E(0) = 0$. Thus the steady state of (2) corresponding to blindness is $\tilde{k}_{in}/\tilde{k}_{out}$. Since acuity decreases as the disease progresses, this implies that

$$\frac{\tilde{k}_{in}}{\tilde{k}_{out}} < \tilde{a}_0. \tag{3}$$

We model E as a product of two factors. With increased exposure to the medication, the body builds up a *tolerance* $T(\tilde{t})$ to the drug. As the tolerance increases, the effectiveness of the drug (even at saturation levels) will decrease. We model this through a *maximum effectiveness factor* $M(T)$, where $M'(T) < 0$. Initially, the patient has no tolerance to the drug, which corresponds to a maximum effectiveness level of M_∞ :

$$T(\tilde{t} = 0) = 0, \quad M(T = 0) = M_\infty. \tag{4}$$

Though the presence of \tilde{C} increases T , in its absence drug clearance will return T to 0. We model these dynamics with a simple forced exponential decay model with rate constant \tilde{k}_∞ :

$$\frac{dT}{d\tilde{t}} = \tilde{k}_T \tilde{C} - \tilde{k}_\infty T, \tag{5}$$

subject to the initial condition in (4). Here \tilde{k}_T is a proportionality constant for the effects of the concentration.

In keeping with our goal of simplicity, we take M to be linear in T , using a Heaviside step function H to ensure that M remains non-negative:

$$M(T) = M_\infty(1 - T)H(1 - T) \equiv M_\infty(1 - T)^+. \tag{6}$$

The second factor in E is the *dosage effectiveness factor* which describes how much of the maximum effectiveness is achieved for a certain concentration \tilde{C} . Mulyukov et al. (2018) use a sigmoidal function, but note that in most of the treatment regime, the medication is at maximum effectiveness. Hence, in order to obtain analytical results, we simplify the sigmoidal curve to a Heaviside function which turns on at some *half-constant* C_* . Substituting this result and (6) into (2), we obtain

$$\frac{d\tilde{a}}{d\tilde{t}} = \tilde{k}_{in} \left\{ 1 + M_\infty(1 - T)^+ H(\tilde{C} - C_*) \right\} - \tilde{k}_{out}\tilde{a}, \quad \tilde{a}(0) = \tilde{a}_0. \tag{7}$$

For later algebraic simplicity, we scale these equations to make them dimensionless. For \tilde{a} , it is natural to normalize by the initial value \tilde{a}_0 . For \tilde{t} and \tilde{C} , we choose k_C and C_* , which have little inter-patient variability (Mulyukov et al. 2018). Substituting our chosen scales

$$a(t) = \frac{\tilde{a}(\tilde{t})}{\tilde{a}_0}, \quad C(t) = \frac{\tilde{C}(\tilde{t})}{C_*}, \quad t = k_C \tilde{t} \tag{8}$$

into (1), (5), and (4), we obtain the following:

$$\frac{dC}{dt} = -C + D \sum_{i=0}^N \delta(t - t_i), \quad C(0) = 0, \quad t_0 = 0, \quad D = \frac{\tilde{D}}{VC_*}, \quad (9)$$

$$\frac{dT}{dt} = k_T C - k_\infty T, \quad T(0) = 0, \quad k_T = \frac{\tilde{k}_T C_*}{k_C}, \quad k_\infty = \frac{\tilde{k}_\infty}{k_C}. \quad (10)$$

Finally, we scale the equation for \tilde{a} , which yields

$$\frac{da}{dt} = k_{in} \{1 + M_\infty(1 - T)^+ H(C - 1)\} - k_{out} a, \quad a(0) = 1, \quad (11a)$$

$$k_{in} = \frac{\tilde{k}_{in}}{\tilde{k}_C \tilde{a}_0}, \quad k_{out} = \frac{\tilde{k}_{out}}{\tilde{k}_C}. \quad (11b)$$

Note from the Heaviside function in (11a) that D must be greater than 1 for the medication to have any efficacy.

We may use (11a) to determine whether a patient will show any improvement initially. With $D > 1$, initially $C > 1$. Then using the given initial conditions for a and T , we may determine the initial derivative of a from (11a):

$$\frac{da}{dt}(0) = k_{in}(1 + M_\infty) - k_{out}.$$

Patients will show improvement initially whenever $da/dt(0) > 0$, i.e., when

$$\frac{k_{in}(1 + M_\infty)}{k_{out}} > 1. \quad (12)$$

Note that all the parameters in (12) are patient-dependent. Physically, with a large value of M_∞ , the maximum effectiveness of the initial dosage is enhanced, leading to initial improvement.

2.2 Analytical solutions

The solution of (9) is easily found using Laplace transform or integrating factor techniques:

$$C(t) = D \sum_{i=0}^N H(t - t_i) e^{-(t-t_i)}. \quad (13)$$

Similarly, the solution of (10) is also easily found to be

$$T(t) = \frac{k_T D}{1 - k_\infty} \sum_{i=0}^N H(t - t_i) \left[e^{-k_\infty(t-t_i)} - e^{-(t-t_i)} \right]. \quad (14)$$

If $k_\infty > 1$, the denominator is less than zero, but so is the bracketed term, yielding the positive value of $T(t)$ desired.

Because of the Heaviside functions in (11a), we may compute our solutions directly up until t_* , which is defined to be the first time for which either of the Heaviside functions switches off. (In other words, either $C(t_*) = 1^+$ or $T(t_*) = 1^-$.) Once $a(t_*)$ has been computed, we can then solve (11a) in the region $t > t_*$ by remembering that in this region, $E(C) = 0$ and there is simple exponential decay. This exponential decay occurs until both of the Heaviside functions are switched on, at which point we solve the full system again with a new initial condition.

For realizable parameter values, $C(t)$ never falls below 1 until the dosing regimen ends (see Fig. 2a below). This is consistent with experimental results, since according to Mulyukov et al. (2018), C decays below 1 only if there are around three months between doses. In the treatment regime under consideration, the furthest spacing between doses is two months.

Hence t_* is determined by whether $T > 1$. We may derive a rough bound on the parameters by noting from (14) that

$$T(t) < \frac{k_T D(N + 1)}{1 - k_\infty} \left(e^{-k_\infty t} - e^{-t} \right). \tag{15}$$

It is a simple exercise in calculus to show that the right-hand side of (15) is bounded above by

$$k_T D(N + 1) k_\infty^{-k_\infty / (k_\infty - 1)}.$$

Bounding the above expression by 1 yields the following bound on k_T :

$$k_T < \frac{k_\infty^{k_\infty / (k_\infty - 1)}}{D(N + 1)}. \tag{16}$$

As D or N increases, the amount of medication in the eye increases, increasing tolerance, and decreasing the bound on k_T . For the values in the Appendix (using medication B), the bound becomes

$$k_T < \frac{9.30 \times 10^{-2}}{(N + 1)}, \tag{17}$$

which is quite tight. Indeed, there are patient cases where T rises above 1, and hence t_* exists (see Fig. 2b below).

Table 1 Base values for dimensionless parameters used in the plots

Dimensionless parameter	Base value
k_∞	0.643
M_∞	1
D	238
k_T	0.001
k_{in}	0.4
k_{out}	0.5

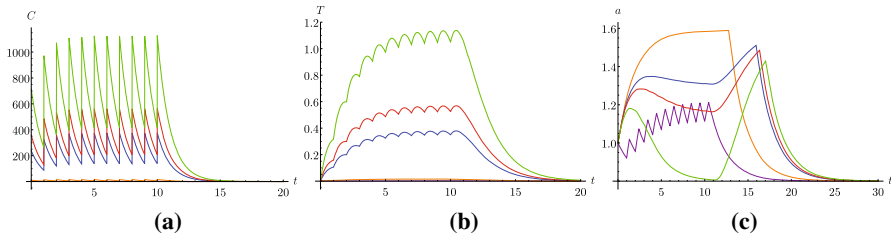


Fig. 2 Plots of **a** the medication concentration C , **b** the body's tolerance T , and **c** the acuity measurement a for varying dosage D : 1 (purple), 10 (orange), 238 (blue), 357 (red), 714 (green). (The last three values are consistent with experiments) (color figure online)

To write the full solution, we take $t_j < \tau < t_{j+1}$. Then Laplace transform or integrating factor techniques yield the solution

$$\begin{aligned}
 a(t) = & \left[1 - \frac{k_{in}(1 + M_\infty)}{k_{out}} \right] e^{-k_{out}t} + \frac{k_{in}(1 + M_\infty)}{k_{out}} \\
 & - \frac{M_\infty k_T k_{in} D}{1 - k_\infty} \sum_{i=0}^j H(t - t_i) \left[\left(\frac{1}{k_{out} - 1} - \frac{1}{k_{out} - k_\infty} \right) e^{-k_{out}(t-t_i)} \right. \\
 & \left. + \frac{e^{-k_\infty(t-t_i)}}{(k_{out} - k_\infty)} - \frac{e^{-(t-t_i)}}{(k_{out} - 1)} \right]. \tag{18}
 \end{aligned}$$

We may plot the solutions of the system (9)–(11) using *Mathematica*. In the following figures, the parameters are given in Table 1, except for the parameter that is varying. These parameters are consistent with parameter fitting to patient data. Note that k_T is quite small, reflecting the slow buildup of tolerance in the body compared to the other biological processes in the system. In each plot, an injection is given at every dimensionless time unit until $t = 10$.

In Fig. 2, we show plots of the concentration, tolerance, and acuity for different values of D . For the high dosages typical of treatment regimes, the concentration remains well above the threshold value 1 between injections. As the dosage increases, the peaks of the concentration increase as expected and tolerance increases as well. (The concentration and tolerance graphs for the two lowest dosages stay near the axis.) The acuity graph with the lowest concentration ($D = 1$) oscillates because

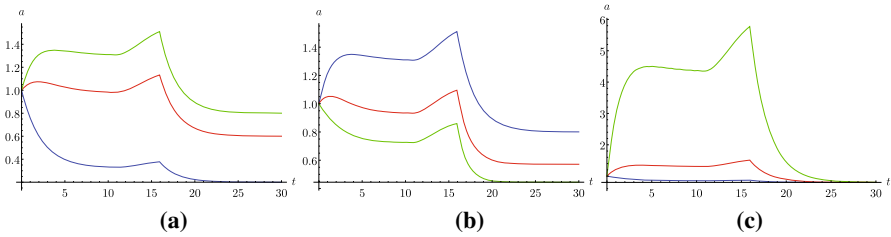


Fig. 3 Plots of the acuity measurement a varying **a** the rate of “inflow” of acuity k_{in} : 0.1 (blue), 0.3 (red), 0.4 (green); **b** the decay rate of acuity k_{out} : 0.5 (blue), 0.7 (red), 0.9 (green); **c** and the largest possible maximum effectiveness factor M_{∞} of the drug: 0.1 (blue), 1 (red), 7 (green) (color figure online)

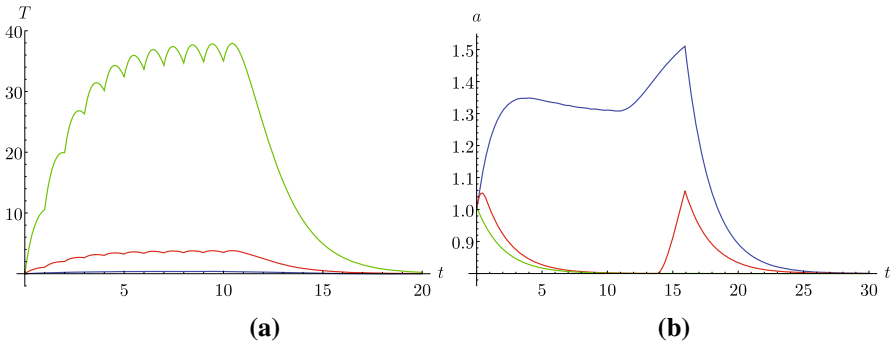


Fig. 4 Plots of **a** the body’s tolerance T and **b** the acuity measurement a varying k_T (coefficient relating increased concentration to tolerance): 0.001 (blue), 0.01 (red), 0.1 (green) (color figure online)

the concentration is low enough that the Heaviside function in (11a) is triggered. For higher values of the concentration, the acuity graph is smooth, increasing for smaller values of C , but then decreasing as the high tolerance inhibits it.

For clinically relevant values of the dosage ($D \geq 238$), we see a characteristic spike *after* the injections end. This is due to the fact that the tolerance is decaying while the concentration remains high enough for the treatment regimen to be effective.

In Fig. 3, we show plots of the acuity for different values of the parameters k_{in} , k_{out} , and M_{∞} , all three of which are patient-specific. (C and T are unaffected by changing these parameters.) The steady state of (11a) in the absence of medication is k_{in}/k_{out} . As acuity declines in the absence of medication, on physical grounds we require that k_{in}/k_{out} should be less than the initial condition 1, which is the dimensionless equivalent of (3).

As expected, we obtain higher acuity when we increase k_{in} (increasing the inflow) or decrease k_{out} (reducing the decay rate). As we increase M_{∞} , the maximum effectiveness of the drug increases, which increases acuity. Moreover, the initial rate of improvement increases, as indicated by (12).

In Fig. 4, we show plots of the tolerance and acuity for different values of k_T . (C is unaffected by changing k_T .) Increasing k_T increases the tolerance for a given C , which in turns reduces the acuity. Note that when k_T is largest, by the time T decays

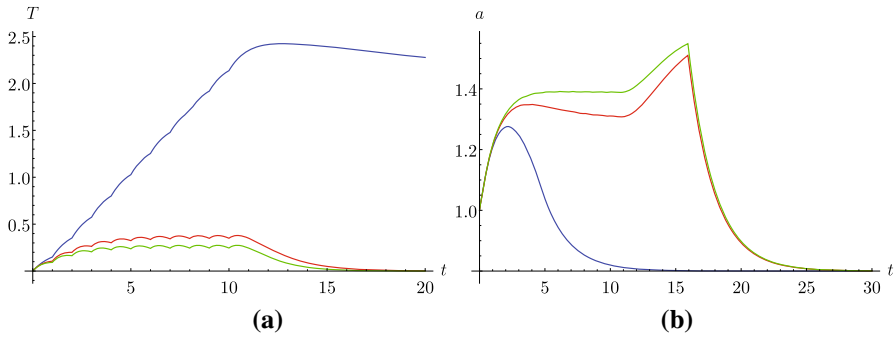


Fig. 5 Plots of **a** the body's tolerance T and **b** the acuity measurement a varying k_∞ (decay rate of tolerance): 0.01 (blue), 0.643 (red), 0.9 (green) (color figure online)

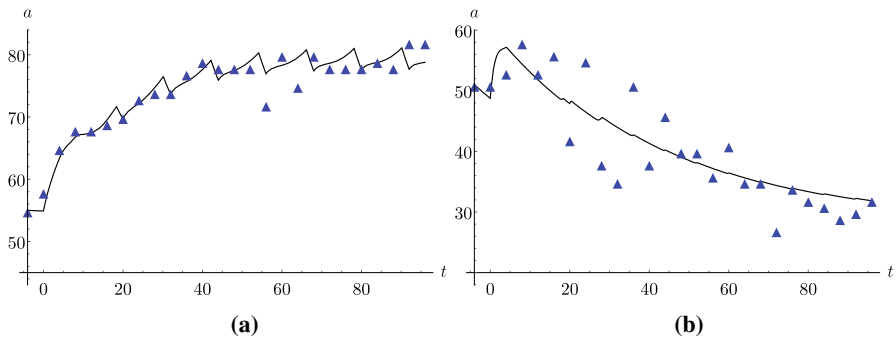


Fig. 6 Curves: optimized trajectory of ODE model for (dimensional) acuity of Patients 28 (left) and 67 (right). The blue triangles indicate when patient measurements were taken. Here the dosage $D = 238$ and the decay rate of tolerance $k_\infty = 0.643$ (color figure online)

below 1, the concentration has decayed away as well, suppressing the post-treatment spike seen for the other values.

In Fig. 5, we show plots of the tolerance and acuity for different values of k_∞ . (C is unaffected by changing k_∞ .) Increasing k_∞ enhances the decay of the tolerance for a given C , which in turn increases the acuity. As in Fig. 4, the slow decay rate of T for the smallest value of k_∞ suppresses the post-treatment spike.

Our model is useful only if it can replicate patient experience. To that end, we fit the model (18) to a few representative curves for BCVA, completely devoid of any patient-specific information. The fitting parameters in the model are the ones which vary amongst patients, namely $\{k_{\text{in}}, k_{\text{out}}, k_T, M_\infty\}$. When fitting, we have used the `FindFit` package in *Mathematica*, which makes use of the Levenberg–Marquardt method for non-linear least squares. The results are shown in Fig. 6, which compares the results from the model with the data from two patients. The curve does exceedingly well at tracking the values for Patient 28 (who responded well to the treatment), while for Patient 67 (who did not respond well), the model captures the general trendline.

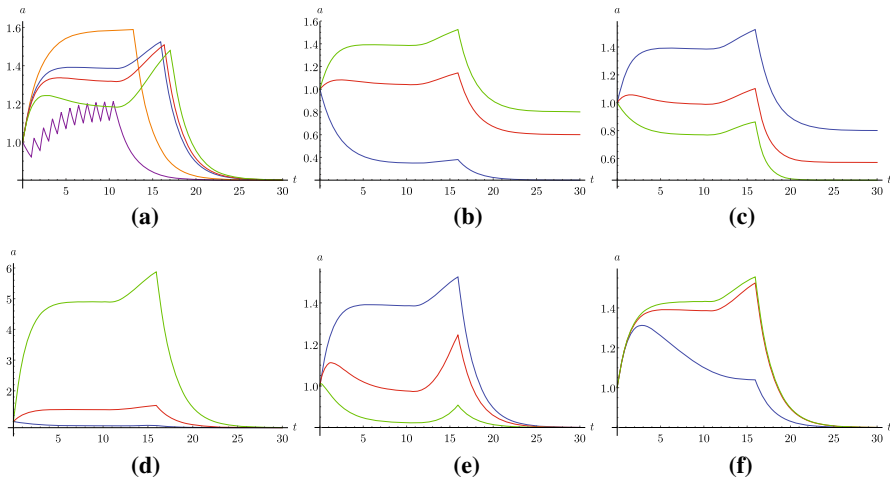


Fig. 7 Plots of the acuity measurement a using (20) and varying a dosage D [1 (purple), 10 (orange), 238 (blue), 357 (red), 714 (green)]; **b** the rate of “inflow” of acuity k_{in} [0.1 (blue), 0.3 (red), 0.4 (green)]; **c** the decay rate of acuity k_{out} : [0.5 (blue), 0.7 (red), 0.9 (green)]; **d** the largest possible maximum effectiveness factor M_{∞} of the drug [0.1 (blue), 1 (red), 7 (green)]; **e** k_T (coefficient relating increased concentration to tolerance) [0.001 (blue), 0.01 (red), 0.1 (green)]; and **f** k_{∞} (decay rate of tolerance) [0.01 (blue), 0.643 (red), 0.9 (green)]. Note the parameter values are the same as in the corresponding Figs. 2, 3, 4 and 5 (color figure online)

In particular, if we define the error quantity for the fit as

$$\frac{1}{N} \sum_{i=1}^N [a_{\text{experimental}}(t_i) - a_{\text{fit}}(t_i)]^2, \tag{19}$$

where a is the *dimensionless* acuity, we obtain values of 1.50×10^{-3} for the graph at left, and 8.00×10^{-3} for the graph at right.

2.3 Other forms

As indicated above, the appeal of such a simple model for $E(C)$ is that analytical solutions with explicit parameter dependence can be easily obtained. Though the solutions have been shown in Fig. 6 to match patient data, such solutions are more useful if they also mimic the results from more realistic models. One such example is to replace (6) with

$$M(T) = \frac{M_{\infty}}{1 + T}, \tag{20}$$

which replicates the behavior of (6) for small T , but which decays to 0 for larger T without the nonsmooth behavior of the Heaviside function. Acuity plots using (20) instead of (6) are shown in Fig. 7. Note that we obtain the same qualitative results.

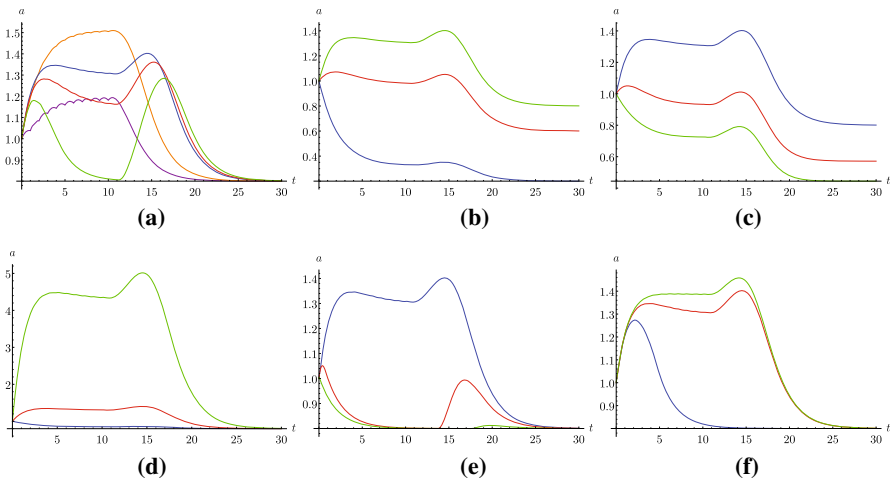


Fig. 8 Plots of the acuity measurement a using (21) and varying **a** dosage D [1 (purple), 10 (orange), 238 (blue), 357 (red), 714 (green)]; **b** the rate of “inflow” of acuity k_{in} [0.1 (blue), 0.3 (red), 0.4 (green)]; **c** the decay rate of acuity k_{out} : [0.5 (blue), 0.7 (red), 0.9 (green)]; **d** the largest possible maximum effectiveness factor M_{∞} of the drug [0.1 (blue), 1 (red), 7 (green)]; **e** k_T (coefficient relating increased concentration to tolerance) [0.001 (blue), 0.01 (red), 0.1 (green)]; and **f** k_{∞} (decay rate of tolerance) [0.01 (blue), 0.643 (red), 0.9 (green)]. Note the parameter values are the same as in the corresponding Figs. 2, 3, 4 and 5 (color figure online)

Similarly, the Heaviside function $H(C - 1)$ for the dosage effectiveness factor in (11a) can be replaced by the sigmoid function in Mulyukov et al. (2018); the dimensionless form is

$$\frac{C}{1 + C}. \quad (21)$$

Again, we are trading analytical tractability for smoothness.

In Fig. 8, we show plots of the acuity using (21). Initially, the qualitative behavior is the same as when using the Heaviside function. However, the graphs are smoother, reflecting the smooth nature of the sigmoid function.

3 A discrete model

3.1 Equations and solutions

Patient data can be collected only at discrete times when they visit the provider. As the treatment regime is designed so that these visits are evenly spaced (usually four weeks apart) (Schmidt-Erfurth et al. 2014), it is convenient to replace the continuous model from Sect. 2 with a discrete dynamical system.

Let C_n be the measurement of the medication at time n (and similarly for a_n and M_n). The first visit is a screening visit where no medication is given. Therefore, for consistency with the definition of time in Sect. 2, we take the screening visit to have

$n = -1$. We work directly with the dimensionless versions of the continuous models; an appropriate discrete analog of (9) is the following:

$$C_{n+1} = \kappa_C C_n + D\delta_{n+1,d}, \quad n \geq -1; \quad C_{-1} = 0, \tag{22a}$$

$$\delta_{n+1,d} = \begin{cases} 1, & \text{dose given at time } n + 1 \text{ (visit } n + 3) \\ 0, & \text{else.} \end{cases} \tag{22b}$$

Without a time scale, we must retain the rate constant for the decay of C . All such terms are denoted κ instead of k to emphasize the structural difference between the two models. Hence the discrete analogs of (10) and (11a) are given by

$$T_{n+1} = \kappa_T C_n + \kappa_\infty T_n, \quad T_{-1} = 0, \tag{23}$$

$$a_{n+1} = \kappa_{in}[1 + M_\infty(1 - T_n)^+ H(C_n - 1)] + \kappa_{out} a_n, \quad a_{-1} = 1. \tag{24}$$

As (22)–(24) are straightforward discrete analogs of the system in Sect. 2, we omit an analysis of variation of solutions on parameter dependence in favor of fitting patient data. To that end, we exploit the functional form of the maximum effectiveness factor to introduce it as a new variable replacing T :

$$M_n = M_\infty(1 - T_n). \tag{25}$$

Making this substitution into (23) and (24), we obtain

$$M_{n+1} = M_\infty - \kappa_T M_\infty C_n - \kappa_\infty(M_\infty - M_n), \quad M_{-1} = M_\infty, \tag{26}$$

$$a_{n+1} = \kappa_{in}[1 + M_n^+ H(C_n - 1)] + \kappa_{out} a_n, \quad a_{-1} = 1, \quad M_n^+ = M_n H(M_n). \tag{27}$$

Note that the Heaviside function is now needed because it is possible for $M_n < 0$, which would correspond to an unphysical effectiveness factor.

To gain insight into the system, we look at the fixed points in two cases: no dosing and regular dosing. In the case of no dosing, (22a) becomes homogeneous and has only the fixed point $C = 0$. Substituting the fixed point $C = 0$ into (26), we obtain a homogeneous equation in the variable $M_\infty - M_n$, which has the fixed point $M = M_\infty$. Lastly, substituting the given fixed points into (27), we have the equation

$$a_{n+1} = \kappa_{in} + \kappa_{out} a_n,$$

which has the single fixed point

$$a^* = \frac{\kappa_{in}}{1 - \kappa_{out}}. \tag{28}$$

Considering the vector (C_n, M_n, a_n) , the Jacobian for the system is given by

$$J = \begin{pmatrix} \kappa_C & 0 & 0 \\ -\kappa_T M_\infty & \kappa_\infty & 0 \\ \kappa_{in} M^+ \delta(C - 1) & \kappa_{in} H(M) H(C - 1) & \kappa_{out} \end{pmatrix}, \tag{29}$$

which has eigenvalues κ_C , κ_∞ , and κ_{out} for *any* fixed point. Therefore, each of these parameters must be bounded between -1 and 1 for stability. And moreover, each must be positive for all the iterates to be positive.

Next, we look at the case of regular dosing at each interval. In that case, (22a) becomes

$$C_{n+1} = \kappa_C C_n + D, \quad (30)$$

which has the fixed point

$$C = \frac{D}{1 - \kappa_C}. \quad (31)$$

Substituting this fixed point into (26), we have

$$M_{n+1} = M_\infty - \kappa_T M_\infty \frac{D}{1 - \kappa_C} - \kappa_\infty (M_\infty - M_n),$$

which has the fixed point

$$M = M_\infty \left[1 - \frac{\kappa_T D}{(1 - \kappa_C)(1 - \kappa_\infty)} \right]. \quad (32)$$

However, since D is large, only for very small κ_T is M going to be positive. This makes biological sense, since regular injections will increase the tolerance beyond the point at which the maximum effectiveness factor goes to 0. Substituting the steady states into (27), we obtain the following:

$$a_{n+1} = \kappa_{\text{in}} [1 + M^+ H(C - 1)] + \kappa_{\text{out}} a_n,$$

where C and M are given in (31) and (32). Hence we have the fixed point

$$a = \frac{\kappa_{\text{in}} [1 + M^+ H(C - 1)]}{1 - \kappa_{\text{out}}}, \quad (33)$$

which will often be the same as (28) because M will most probably be negative. In any case (33) is stable under the conditions listed above.

We may solve analytically for C_n in the case of regularly spaced injections as follows. The general solution of (30) is given by

$$C_{n+1} = \frac{D}{1 - \kappa_C} + \alpha \kappa_C^n, \quad (34)$$

where α is an arbitrary constant. Suppose that injections are given during P injection periods at times $n \in [n_{p-}, n_{p+}]$ for $p = 1, 2, \dots, P$, and let $n_{1-} = 0$. Then using

the general solution (34) for any dosing interval $[n_{p-}, n_{p+}]$, the contribution to the total C_n from the dosing term is given by the following:

$$\frac{D}{1 - \kappa_C} (1 - \kappa_C^{n+1-n_{p-}}), \quad n \in [n_{p-}, n_{p+}]. \tag{35}$$

After it ends, the contribution from that dosing interval is just continually reduced by the factor κ_C :

$$\frac{D}{1 - \kappa_C} (\kappa_C^{n-n_{p+}} - \kappa_C^{n+1-n_{p-}}), \quad n \geq n_{p+}. \tag{36}$$

Combining these terms for all dosing intervals yields the full solution in this region:

$$C_n = \frac{D}{1 - \kappa_C} \sum_{p=1}^P H(n - n_{p-}) (1 - \kappa_C^{n+1-n_{p-}}) - H(n - (n_{p+} + 1)) [1 - \kappa_C^{n+1-(n_{p+}+1)}]. \tag{37}$$

Equation (37) can be explained as follows. The first term represents the solution for constant dosing, starting at n_{p-} . To shut the dosing off, we just subtract off another term for constant dosing, starting at $n = n_{p+} + 1$, which is the first period after the end of the real dosing.

3.2 Data fitting

We can use the results from the discrete model to fit actual patient data. Values of D and κ_∞ are listed in the [Appendix](#); the t_i can be determined from the data. Thus the parameters to be fit are κ_{in} , κ_{out} , κ_T , and M_∞ ; such quantities should vary with each patient (Mulyukov et al. 2018). Given the large size of D , from (10) we expect that our parameter fit should have $\kappa_T \ll 1$ to prevent the tolerance from becoming very large very quickly.

The data is rather noisy and in some instances there is not a monotonically positive response to the drug. In fact, a patient may continually get worse despite receiving regular doses. Our goal was to find optimal values for $\{\kappa_{in}, \kappa_{out}, \kappa_T, M_\infty\}$ for each of the 103 test patients. After the parameters were fit for each patient, we also sought to determine if any values of κ_{in} or κ_{out} were characteristic of responsive or non-responsive patients.

To visualize our results, we run the model using the dosage schedule of Patient 6 with a demonstrative chosen set of parameter values. The results are shown in Fig. 9. As in the continuous model, the concentration of the drug oscillates due to the frequency of the doses. When a dose occurs, the concentration is at a local maximum, and then declines in the four weeks between visits. The blue line corresponds to the threshold value $C = 1$; as in the continuous case, the concentration rarely dips below the threshold while medication is being administered.

In the plot of M_n , the maximum effectiveness decreases after every dose, suggesting that tolerance is increasing and limiting the body’s response to the drug. The acuity

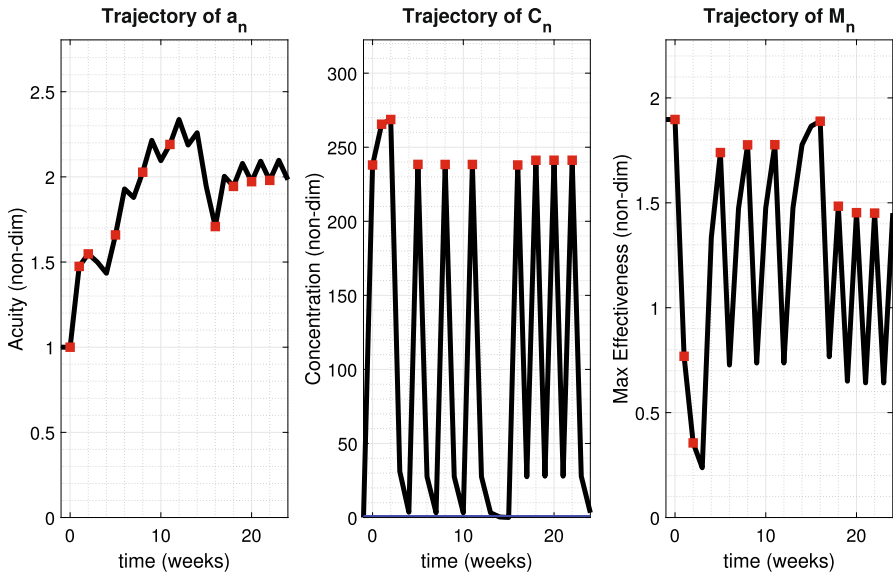


Fig. 9 Left: experimental measurements of the acuity measurement a_n for an individual patient. Red blocks indicate when a dose was administered. Middle and right: trajectories of concentration C_n and maximum effectiveness factor M_n with fixed parameters given in the Appendix (dosage schedule B) and fit parameters as follows: acuity “inflow” rate $\kappa_{in} = .25$, acuity decay rate $\kappa_{out} = .75$, coefficient relating increased concentration to tolerance $\kappa_T = 0.0025$, and largest possible maximum effectiveness factor $M_\infty = 1.8972$ (color figure online)

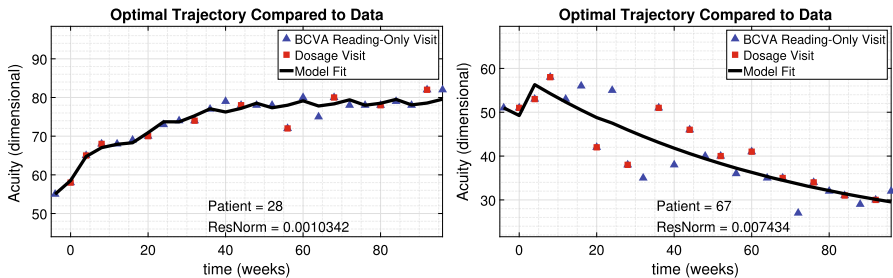


Fig. 10 Optimized trajectory for (dimensional) acuity of Patients 28 (left) and 67 (right). The model does well to fit both responsive and non-responsive patients

a_n increases after every dose, and then decays in the intervening weeks. In particular, between weeks 12 and 16 (when the patient missed a dose), the acuity declines more dramatically than usual.

Using MATLAB’s built-in `lsqnonlin` function, we optimized the four parameters for every patient in the given data set. Because this solver inputs an initial parameter set, we also implemented MATLAB’s global optimization function `multistart` with 100 other initial conditions to avoid local maxima in the optimization function.

We compare acuity results of the discrete model with patient data in Fig. 10, which uses the same patients as in Fig. 6. In contrast to the relatively smooth nature of the

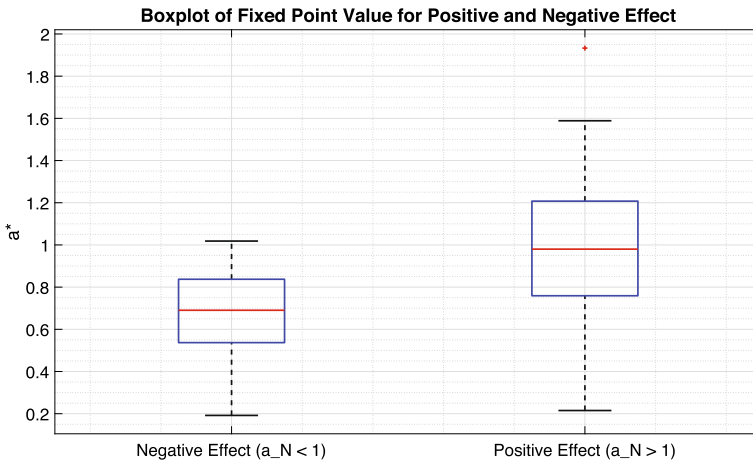


Fig. 11 Box plot of a^* values for nonresponsive (negative) and responsive (positive) patients

fits from the ODE model, the discrete model's ability to track smaller-scale features of the acuity depends on their amplitude. For patient 28, most of the individual data points oscillate within a narrow band about a general trendline, and the model is able to follow those oscillations. However, in patient 67, the oscillations are much wilder (at least initially), and the model follows only the general trendline. These results track those from the ODE model shown in Fig. 6.

Obviously, it is desirable for the model to fit the individual oscillations. However, the important clinical variable is much cruder: whether or not a particular patient responds to treatment. To interpret our results quantitatively, we define patients who are unresponsive to treatment to have $a_N < 1$. (In other words, even after treatment, the final acuity measurement was less than the initial value.) Similarly, we define responsive patients as those who have $a_N > 1$. Once we had optimized the parameters for each patient in the given data set, we calculated their respective values of a^* as defined in (28). Recall that this is the fraction of acuity the patient would expect to retain in the absence of any treatment.

Our results are shown in a box plot in Fig. 11. At left, the unresponsive patients are clustered at values that are much smaller than 1 (statistically less than 1 with $> 99\%$ confidence). Biologically, their response in the absence of medication would be so poor that the treatment regime does not help enough to drive $a_N > 1$. In contrast, the responsive patients at right are clustered near $a^* = 1$. Hence the added benefit from the medication can not only slow the patient decline, but also improve their acuity long-term.

Figure 11 also suggests a way to evaluate the efficacy of the treatment regime before its completion. In particular, the curve fitting needed to calculate a^* can be redone each time an acuity reading is taken. If several consecutive estimates provide a value of $a^* < 3/4$, it is more likely than not that the patient will fall into the unresponsive category. The clinician can then use this information (in conjunction

Without boundaries, the relevant equation can be written in symmetric spherical coordinates as

$$\frac{\partial \tilde{C}}{\partial \tilde{t}} = -k_C \tilde{C} + \frac{\tilde{D}}{\tilde{r}^2} \frac{\partial}{\partial \tilde{r}} \left(\tilde{r}^2 \frac{\partial \tilde{C}}{\partial \tilde{r}} \right), \tag{39a}$$

where \tilde{r} is the spherical coordinate. Equation (39a) replaces (1). Note the decay of medication is assumed uniform throughout the domain. We note that in their work, Zhang et al. (2018) include pressure-driven convection in the vitreous along with diffusion. However, as the pressure gradients driving such flow last for only around 30 min after injection (Falkenstein et al. 2007; Zhang et al. 2018), over the four weeks between doses, diffusion effects obviously dominate.

We begin by examining the case of a single injection at time $\tilde{t} = 0$. Given the assumed geometry, this leads to the following initial condition:

$$\tilde{C}(\tilde{r}, 0) = \tilde{D} \delta(\tilde{r}). \tag{39b}$$

The scalings for \tilde{C} and \tilde{t} are given by (8), and for the radius we let

$$r = \frac{\tilde{r}}{R_e}. \tag{40}$$

Making these substitutions, we obtain

$$\frac{\partial C}{\partial t} = -C + \frac{D}{r^2} \frac{\partial}{\partial r} \left(r^2 \frac{\partial C}{\partial r} \right), \quad D = \frac{\tilde{D}}{R_e^2 k_C}, \tag{41a}$$

$$C(r, 0) D_d \delta(r), \quad D_d = \frac{\tilde{D}}{R_e^3 C_*}. \tag{41b}$$

The decay in (13) motivates the substitution

$$C(r, t) = e^{-t} u(r, t), \tag{42}$$

which reduces (41a) to the standard heat operator. Given that we have assumed an infinite domain, the solution is given by the fundamental solution, multiplied by the dosage strength D_d :

$$C(r, t) = \frac{D_d}{(4\pi Dt)^{3/2}} \exp\left(-\frac{r^2}{4Dt} - t\right). \tag{43}$$

The relevant concentration is at the retina, which is at a dimensional length \tilde{R}_d from the source (see Fig. 12). Hence we compute

$$C(R_d, t) = \frac{D_d}{(4\pi Dt)^{3/2}} \exp\left(-\frac{R_d^2}{4Dt} - t\right), \tag{44}$$

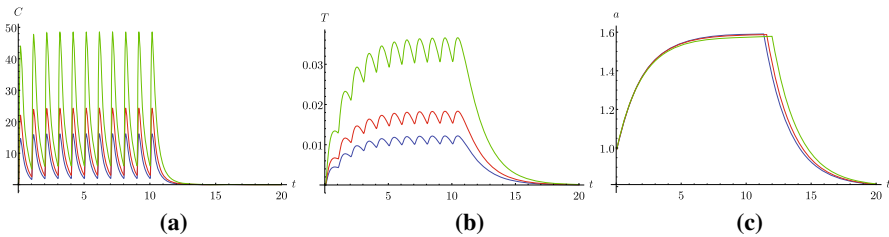


Fig. 13 Plots of **a** the medication concentration C , **b** the body’s tolerance T , and **c** the acuity measurement a for varying dosage D_d : 487 (blue), 732 (red), 1461 (green). Here, $\mathcal{D} = 1.44$, $R_d = 1.39$ (color figure online)

where the dimensionless R_d is defined similarly to (40).

To introduce the effects of multiple injections, we note that since the problem is linear, we may just shift time from t to $t - t_i$, and the solution remains the same. Hence in the full case we obtain

$$C(R_d, t) = \frac{D_d}{(4\pi\mathcal{D})^{3/2}} \sum_{i=0}^N \frac{H(t - t_i)}{(t - t_i)^{3/2}} \exp\left(-\frac{R_d^2}{4\mathcal{D}(t - t_i)} - (t - t_i)\right), \quad (45)$$

which replaces (13) in computations of T and a .

To complete the solution, we must compute the distance R_d to be traversed. Per Frenkel et al. (2010), the insertion site is taken to be an arc-length distance R_p (the subscript “p” is for “position”) from the edge of the limbus, which is a structure near the iris with cross-sectional radius R_l (the subscript “l” stands for “limbus”; see Fig. 12). The needle is injected a distance R_i (the subscript “i” is for “injection”) into the eye and the medicine is released. In Fig. 12, we show the needle directed toward the center of the eye. It is also possible that the needle is directed more towards the retina (Frenkel et al. 2010), which would shorten the path. However, as we are looking to quantify the maximum effect of diffusion, we consider the route with the longest path.

The computation is a tedious exercise in trigonometry and the Law of Cosines; the final result is

$$R_d^2 = 1 + (1 - R_i)^2 - 2R_i \cos \theta_*, \quad (46a)$$

$$\cos \theta_* = R_l \sin R_p - \sqrt{1 - R_l^2} \cos R_p. \quad (46b)$$

A graph of (45) for the parameters in the Appendix is shown in Fig. 13, which is analogous to Fig. 2, though with some differences. The peak concentration is an order of magnitude smaller, since the medication must spread throughout the eye. This then forces the tolerance to be very small, but with oscillations due to the spikes in the concentration. Given that the variation in the tolerance is so small, the acuity follows the smooth exponential profile consistent with the lowest dosage in Fig. 2.

Figure 14 is analogous to Fig. 7. The behavior of the acuity as the parameters change remains the same, but with the smaller peak concentration, there are no discernible

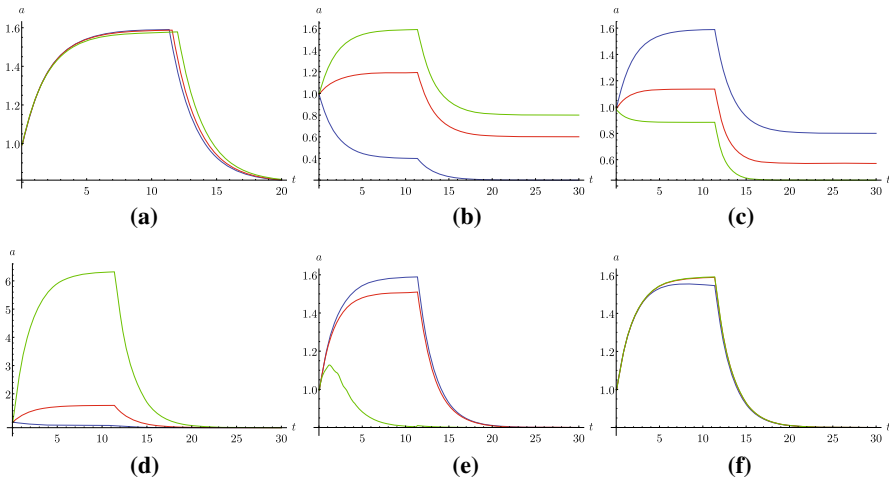


Fig. 14 Plots from the PDE model of the acuity measurement a using (45) and varying **a** dosage D_d [487 (blue), 732 (red), 1461 (green)]; **b** the rate of “inflow” of acuity k_{in} [0.1 (blue), 0.3 (red), 0.4 (green)]; **c** the decay rate of acuity k_{out} : [0.5 (blue), 0.7 (red), 0.9 (green)]; **d** the largest possible maximum effectiveness factor M_∞ of the drug [0.1 (blue), 1 (red), 7 (green)]; **e** k_T (coefficient relating increased concentration to tolerance) [0.001 (blue), 0.01 (red), 0.1 (green)]; and **f** k_∞ (decay rate of tolerance) [0.01 (blue), 0.643 (red), 0.9 (green)]. Parameter values for **b–f** are the same as in the corresponding Figs. 2, 3, 4 and 5. Here, $\mathcal{D} = 1.44$, $R_d = 1.39$ (color figure online)

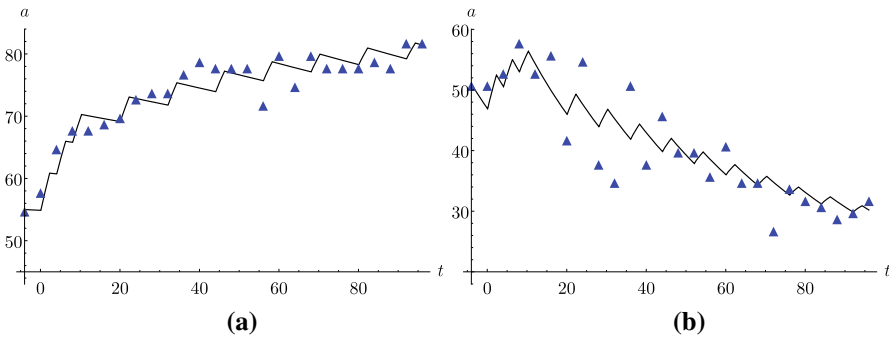


Fig. 15 Curves: optimized trajectory of PDE model for (dimensional) acuity of Patients 28 (left) and 67 (right). The blue triangles indicate when patient measurements were taken. Here, $\mathcal{D} = 1.44$, $R_d = 1.39$, $D_d = 487$, $k_\infty = 0.643$ (color figure online)

oscillations. The only exceptional profile is the case of highest k_T in subfigure (e). In this case, the tolerance does grow large even in the presence of the smaller peak in C , driving down the acuity even during dosage administration.

In order to qualify our model, we compare acuity results from the PDE model with patient data in Fig. 15, which uses the same patients as in Fig. 6. We fit for the same parameters: $\{k_{in}, k_{out}, k_T, M_\infty\}$. Using the same error definition as in (19), we have an error of 1.78×10^{-3} for the figure on the left, and 8.19×10^{-3} for the figure on the right. We have again used the *Mathematica* package to produce the plots. Note

from Fig. 6 that the PDE model does just as well as the ODE model for the responsive patient 28, and is superior for the non-responsive patient 67.

4.2 Finite model

While the infinite-extent model is simple and analytically tractable, it is obviously not reflective of the biological reality. In particular:

1. As shown in Fig. 12, the eyeball clearly is a finite domain, and there is a loss of spherical symmetry since the injection site I is not in the center.
2. The medication does not decay uniformly throughout the eye, as modeled in (41a). Though there may be a small amount of degradation within the vitreous itself (del Amo et al. 2017), most of the medication loss is through transport through the surface of the vitreous to other portions of the eye (Zhang et al. 2018).

To address some of these shortcomings, we replace the dimensionless transport equation (41a) with

$$\frac{\partial C}{\partial t} = \mathcal{D}\nabla^2 C, \quad 0 \leq |\mathbf{r}| \leq 1, \quad (47a)$$

which introduces a spherical boundary for the eye centered about the origin. It also removes the decay from within the eye itself; instead, we introduce medicine leakage into the aqueous layer and episcleral vein by adding a thin spherical shell of width h to the exterior of the sphere:

$$\frac{\partial C_s}{\partial t} = \mathcal{D}_s \nabla^2 C_s, \quad 1 \leq |\mathbf{r}| \leq 1 + h; \quad \mathcal{D}_s < \mathcal{D}, \quad (47b)$$

where the subscript “s” refers to “shell”. This shell will serve the same function as the Robin boundary condition in Zhang et al. (2018) to remove concentration from the vitreous layer. The fact that $\mathcal{D}_s < \mathcal{D}$ indicates that leakage from the vitreous to the other layers is slow.

We then require that

$$C_s(r = 1 + h) = 0, \quad (48)$$

which ensures that there is no medication outside of the shell. Requiring continuity of concentration and flux at the interface $r = 1$ yields a full set of boundary conditions. By taking the injection axis as the z -axis as in Fig. 12, the initial condition (41b) is replaced by

$$C(r, \theta, 0) = \frac{2}{r^2 \sin \theta} D_d \delta(r - (1 - R_i), \theta), \quad (49)$$

where we use the convention that θ is the polar angle. (The factor of 2 is needed since the injection is at one of the boundaries in the azimuthal angle.) Note from the form of (49) that the full problem is symmetric in the azimuthal angle.

Using separation of variables, we obtain the following solution modes for C and C_s :

$$C = \exp(-\mathcal{D}\lambda^2 t) f_l(r) P_l(\cos \theta), \quad 0 \leq r \leq 1, \tag{50a}$$

$$C_s = \exp(-\mathcal{D}_s\mu^2 t) f_l(r) P_l(\cos \theta), \quad 1 \leq r \leq 1 + h, \tag{50b}$$

$$f_l(r) = \begin{cases} f_<(r) = j_l(\lambda r), & 0 \leq r \leq 1, \\ f_>(r) = \alpha j_l(\mu r) + \beta y_l(\mu r), & 1 \leq r \leq 1 + h. \end{cases} \tag{50c}$$

where P_l is the l th Legendre polynomial, and j_l and y_l are the spherical Bessel functions. For these modes to solve the full system, their time-varying behavior must match across $r = 1$; hence

$$\mathcal{D}\lambda^2 = \mathcal{D}_s\mu^2. \tag{51}$$

The continuity and boundary conditions apply only to f_l ; they may be written as a homogeneous system as follows:

$$M_l \begin{pmatrix} \alpha \\ \beta \\ 1 \end{pmatrix} = \mathbf{0}, \quad M_l = \begin{pmatrix} -j_l(\mu) & -y_l(\mu) & j_l(\lambda) \\ -\mathcal{D}_s\mu j'_l(\mu) & -\mathcal{D}_s\mu y'_l(\mu) & \mathcal{D}\lambda j'_l(\lambda) \\ j_l(\mu(1+h)) & y_l(\mu(1+h)) & 0 \end{pmatrix}. \tag{52}$$

Equation (52) has a nontrivial solution only for those values of $(\lambda_{l,i}, \mu_{l,i})$ satisfying (51) and $\det M_l = 0$, and those values are the eigenvalues of the system. These eigenvalues will then determine a set of eigenfunctions $f_{l,i}(r)$.

Performing direct computation using the parameters in the [Appendix](#), we find that the two lowest eigenvalues are given by

$$\lambda_{0,1} = 0.141, \quad \lambda_{1,1} = 0.659. \tag{53}$$

Note that the second mode decays much more quickly than the first. A plot of $f_{0,1}(r)$ is shown in Fig. 16. Note that due to the large discrepancy between \mathcal{D} and \mathcal{D}_s , the leading-order eigenfunction approximates a no-flux condition at $r = 1$.

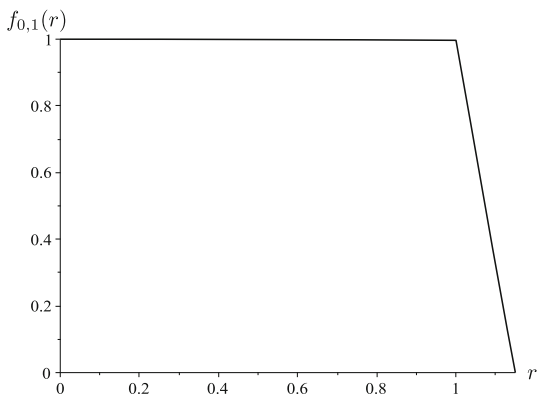
From standard Sturm-Liouville theory, the full solution may be written as

$$C(r, \theta, t) = \sum_{l=0}^{\infty} \sum_{i=1}^{\infty} \gamma_{l,i} \exp(-\mathcal{D}\lambda_{l,i}^2 t) P_l(\cos \theta) f_{l,i}(r), \tag{54a}$$

where $f_{l,i}(r)$ is given by (50c) with (λ, μ) replaced by $(\lambda_{l,i}, \mu_{l,i})$, and the $\gamma_{l,i}$ are determined by the initial condition. As this is a δ -function, the computation is straightforward, yielding

$$\gamma_{l,i} = \frac{D_d j_l(\lambda_{l,i}(1 - R_i))}{\|P_l(\cos \theta)\|^2 \|f_{l,i}(r)\|^2}. \tag{54b}$$

Fig. 16 Plot of first eigenfunction $f_{0,1}(r)$ versus r . Note that it is almost identically constant throughout the eyeball



where we have used (50c). The θ normalization factor is easily found to be (Bell 1968)

$$\|P_l(\cos \theta)\|^2 = \frac{2}{2l + 1}. \tag{55}$$

To calculate the r normalization factor, we begin by noting that any solution y of the spherical Bessel operator with parameters (l, λ) satisfies

$$\frac{dQ}{dr} = 2\lambda^2 r^2 y^2, \tag{56a}$$

$$Q(r, y, \lambda) = r \left(r y' + \frac{y}{2} \right)^2 + \lambda^2 r^3 y^2 - \left(l + \frac{1}{2} \right)^2 r^2 y^2. \tag{56b}$$

The normalization factor we want is given by

$$\begin{aligned} \|f_{l,i}(r)\|^2 &= \int_0^1 r^2 f_{<}(r)^2 dr + \int_1^{1+h} r^2 f_{>}(r)^2 dr \\ &= \frac{1}{2\lambda^2} [Q(r, f_{<}, \lambda_{l,i})]_0^1 + \frac{1}{2\mu^2} [Q(r, f_{>}, \mu_{l,i})]_1^{1+h}, \end{aligned} \tag{57}$$

where we have used the fact that $f_{>}$ satisfies the spherical Bessel operator with parameter μ . Note that the integral must be broken up into two pieces due to the discontinuity in the diffusion coefficient.

By the definition of Q in (56b) we have that $Q(0, f_{<}, \lambda) = 0$, and by satisfying (48) we see that only the derivative terms will remain in $Q(1+h, f_{>}, \mu_{l,i})$. The terms at $r = 1$ may be simplified somewhat by using the required matching and continuity conditions, as well as (51). After working through much tedious algebra, the final expression is

$$\|f_{l,i}(r)\|^2 = \frac{1}{2\mu_{l,i}^2} \left\{ \left[\left(\frac{D_s}{D} - 1 \right) (f'_{>})^2 - \left(\frac{D}{D_s} - 1 \right) l(l+1) f_l^2 \right]_{r=1} \right\}$$

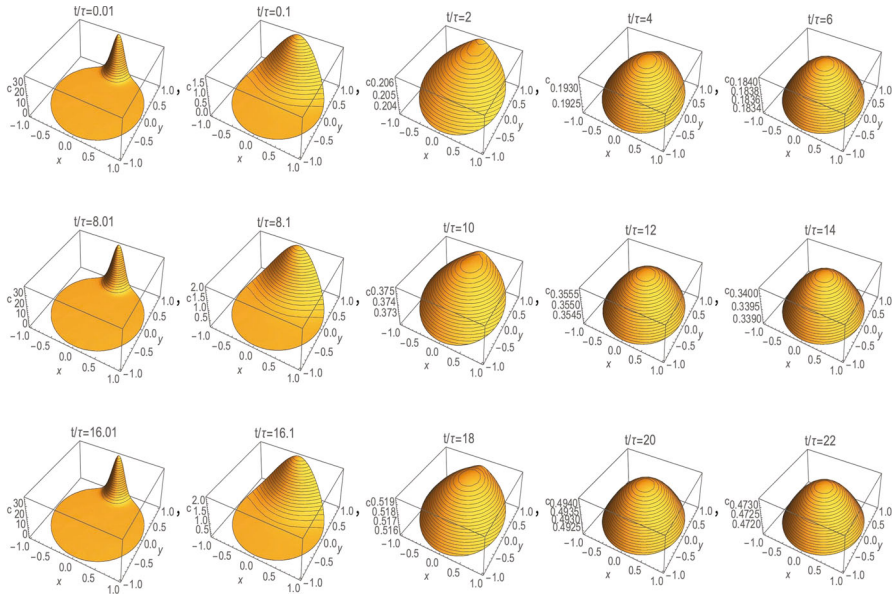


Fig. 17 Plot of $C(r, \theta, t)/D_d$ in cross section through origin and z -axis with repeated doses given at $t_i/\tau = 8i$, $\tau = 1/D$

$$+(1 + h)^3 [f'_l(1 + h)]^2 \}. \tag{58}$$

Note that if \mathcal{D} were equal to \mathcal{D}_s , then the first bracketed term would vanish and we would obtain only boundary terms, which is more standard for a Sturm-Liouville problem.

With the geometry in Fig. 12, the target area has $(r, \theta) = (1, \theta_*)$. Therefore, upon substituting (55) into (54) at those coordinates, we obtain

$$C(1, \theta_*, t) = \sum_{l=0}^{\infty} \sum_{i=1}^{\infty} \frac{(2l + 1) D_d j_l(\lambda_{l,i} (1 - R_i)) j_l(\lambda_{l,i}) \exp(-\mathcal{D} \lambda_{l,i}^2 t) P_l(\cos \theta_*)}{2 \|f_{l,i}(r)\|^2}. \tag{59}$$

For multiple injections we can use linearity and the Markovian property to find the solution:

$$C(1, \theta_*, t) = \sum_{i=0}^N H(t - t_i) C(1, \theta_*, t - t_i), \tag{60}$$

where C on the right-hand side is given by (59). Equation (60) is analogous to (45).

We present computational results in Fig. 17 using the parameters in the Appendix and with injections given at every 8 units of time $\tau = 1/D$. The results contain l -modes up to 100 and eigenvalues up to $\lambda = 21$. (Note from (59) that the contribution from

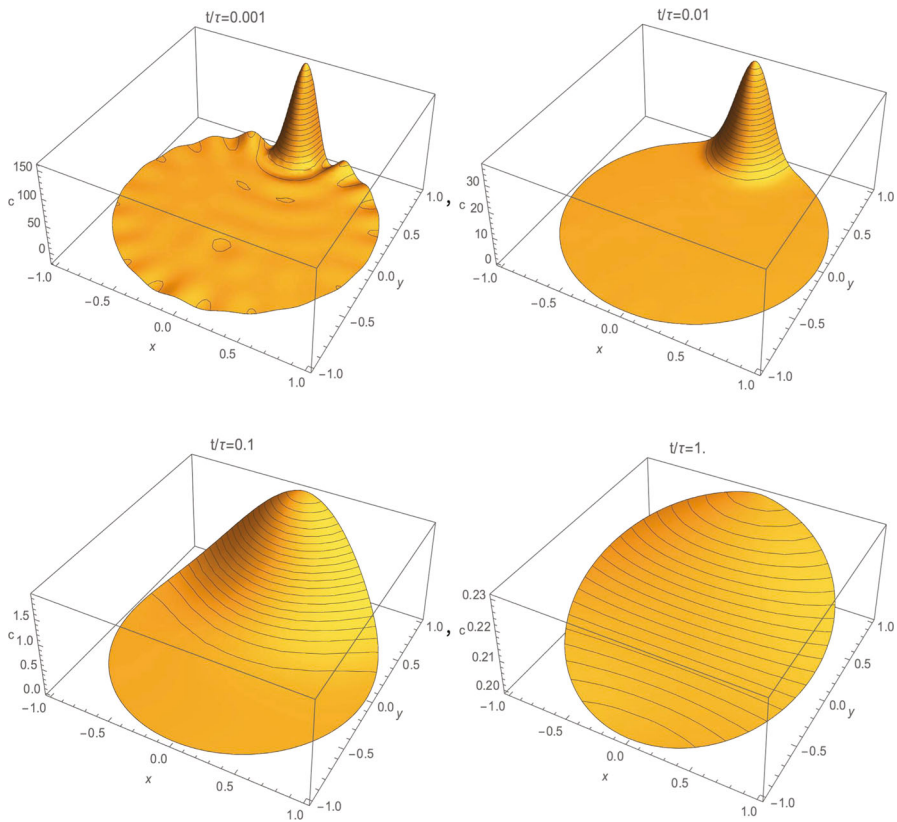


Fig. 18 Plot of $C(r, \theta, t)/D_d$ at $t/\tau = 0.001, 0.01, 0.1, 1.0$, $\tau = 1/D$ in cross section through origin and z -axis. (The dosage D_d is delivered at $t = 0$ at a point with $r = (1 - R_i)$, $R_i = 0.9$, $\theta = 0$)

these modes will be incredibly tiny.) We plot consecutive snapshots of the solution for times $t < 22\tau$. Since there is no polar angle dependence, we plot C in a cross section of a plane through the origin and the z -axis; the domain is thus a circle $x^2 + y^2 < 1$. Injections are delivered as described in (49).

We cannot accurately plot the solution right after the injection as it has a sharp peak and, with finite number of modes included, oscillates a lot; however it can be accurately plotted after some delay after the injection, as high modes become exponentially suppressed. Such near-injection plots are shown in Fig. 18.

The volume-averaged concentration of the lowest mode of the solution right after a unit dose injection is 0.2058. This is roughly the concentration which survives a few units of time after the injection, as this mode decays slowly while other modes are exponentially suppressed after that amount of time. If another injection is delivered before the lowest mode leaks, it will roughly double the concentration surviving after higher modes become suppressed.

As discussed above, when t is near t_i , one must compute many modes of (59) to accurately represent the solution (which will have a sharp peak at the injection site).

However when $t - t_i$ is not small, the contribution from modes with large eigenvalues is strongly suppressed.

In particular, without subsequent injections the solution approaches $C = 0$ (as imposed by the outer Dirichlet condition) at an exponential rate, with the slowest decaying mode corresponding to the lowest eigenvalue. The discrepancy in the sizes of the eigenvalues in (53) indicates that the mode with $l = 0, i = 1$ dominates. Recalling that

$$j_0(r) = \frac{\sin r}{r}, \quad y_0(r) = -\frac{\cos r}{r},$$

we may rewrite f_0 as

$$f_0(r) = \begin{cases} \frac{\sin(\lambda r)}{\lambda r}, & 0 \leq r \leq 1, \\ -\frac{\sin \lambda}{\sin(\mu h)} \frac{\sin(\mu(r-(1+h)))}{\lambda r}, & 1 \leq r \leq 1 + h, \end{cases} \tag{61}$$

where

$$\mathcal{D}(\lambda \cot \lambda - 1) = -\mathcal{D}_s(\mu \cot \mu h + 1). \tag{62}$$

Equation (62) is the analog of taking $\det M_0 = 0$ in (52).

Substituting (61) into the leading-order term ($l = 0, i = 1$) of (59) and (58), we have

$$C(1, \theta_*, t) \sim \frac{D_d \sin \lambda_{0,1}(1 - R_i) \sin(\lambda_{0,1}) \exp(-\mathcal{D}\lambda_{0,1}^2 t)}{2\lambda_{0,1}^2(1 - R_i)\|f_{0,1}(r)\|^2}, \tag{63a}$$

$$\|f_{0,1}(r)\|^2 = \frac{\sin^2 \lambda_{0,1}}{2\mu_{0,1}^2 \lambda_{0,1}^2} \left\{ \left(\frac{D_s}{D} - 1 \right) [\mu_{0,1} \cot(\mu_{0,1}h) + 1]^2 + \frac{(1+h)\mu_{0,1}^2}{\sin^2(\mu_{0,1}h)} \right\}. \tag{63b}$$

However, we reiterate that this expression is valid only for times sufficiently removed from times of injections.

5 Conclusions and further research

5.1 Discussion

Anti-VEGF treatments have shown great promise for treatment and symptom relief for patients with nAMD; however not all patients respond uniformly. Understanding the body’s response, based on well-established clinical measures (e.g., BCVA and CSFT) early in the course of treatment, would allow practitioners to optimize and adjust the treatment regimen. The goal of this manuscript was to test various mathematical approaches in modeling the evolution of these clinical measurements with medication delivered at regular intervals and to seek explicit analytical solutions of those models.

Because of this goal, various assumptions and simplifications were made. We worked with a continuous ODE model that is similar in nature to the model provided in the literature by Mulyukov et al. (2018); however, it is simplistic enough to obtain an explicit solution. We also considered a simplified discrete analog of the ODE model that focuses more on the discrete nature of the treatment regime, and thus is more applicable to specific patient data. Lastly, we considered a spatial component to the model which effectively models the diffusion of the medication within the eye. We discuss the effectiveness of each model below.

Using the ODE model presented by Mulyukov et al. (2018) as a starting point, we sought to develop a model for which a tractable analytical solution is possible, while also taking into account the patient-specific treatment regime. We successfully derived a model with analytical solutions using identical dynamics for the acuity level over time; however, we took a different approach in modeling the concentration and effectiveness of the drug. Concentration of the drug is modeled as an exponential decay with monthly increases based on the treatment schedule, thus resulting in a series of Heaviside functions. We simplify our model greatly by using Heaviside functions for tolerance and maximum effectiveness, which allows us to derive an analytical solution for BCVA over time. The periodic nature of the treatment regime dictates a series solution and allows us to personalize the model to patient data.

Using our explicit solution, we can analyze the parameter dependence more easily and perform a sensitivity analysis on important model parameters. We performed a preliminary study on the output of the model as key parameters were varied. The maximum effectiveness parameter (M_∞) controls the rate of improvement due to the initial treatment. The dosage parameter (D) controls the levels of drug concentration, which usually remain well above the threshold for maximum effectiveness, which is characteristic of the model in Mulyukov et al. (2018). In short, our results show that the model acts as it should, under the fundamental assumption that acuity increases with treatment of anti-VEGF. Furthermore, our model can be viewed as a simplified base model. We sacrifice smoothness for simplicity, but different functions for the tolerance and maximum effectiveness can be exchanged to test the efficiency and accuracy of different models. Nevertheless, we were able to predict the outcome of the BCVA score for patients over time. In Sect. 2.3, we replace the concentration function with first-order elimination pharmacokinetics to simulate the results of Mulyukov et al. (2018). Overall, our model can be manipulated to test acuity output based on different reaction kinetics, but analytical solutions will be sacrificed.

We adapted the ODE model into a discrete system so that we may better predict the outcome of the BCVA score for patients' monthly visits. Because the data is in time series form without information between visits, a discrete model may better describe the acuity at these distinct time points. A full solution to the model is possible assuming regular dosing. Our main goal for this model was to fit the parameters κ_{in} and κ_{out} to the patient data since these two parameters dictate the acuity at the end of the treatment regime. We successfully accomplished this task using a global optimization technique in MATLAB.

The model effectively captures the general trend of acuity for both responsive and non-responsive patients. Moreover, by examining the single parameter a^* (which is a combination of the fit parameters κ_{in} and κ_{out}), we were able to establish predictions

for when the treatment regime would be successful. Although the model is simple and does well to describe the progression of acuity with time, a better definition of responsiveness or a more robust optimization technique may be needed to gain further insight into how these parameters describe patients' overall responsiveness to the treatment.

Finally, we study a continuum PDE model, which takes into account that the concentration of medicine in the vitreous humor is not uniform; medication is delivered to a small volume around the injection site and has to spread to the boundary of the vitreous humor and to the other compartments. An approach that considers the spatial aspects of the biology clearly offers advantages over compartmental models. It has to be noted that the PDE model uses an idealized geometry: the vitreous humor is taken to be spherical, with other compartments modeled by an outer layer with lower diffusion coefficient, followed by a sink further out. In addition, we treat diffusion as the only transport mechanism.

Nevertheless, this setting allows for an analytic solution, which means, in particular, that computational complexity is not dramatically increased compared to ODE multi-chamber models. Moreover, we do not require sophisticated PDE solvers, as are needed for the more complicated models in Zhang et al. (2018), which use additional transport mechanisms and clearance parameters. Another advantage of an analytic solution is that it provides a clear explanation for the exponential decay observed in Gadkar et al. (2015) and Hutton-Smith et al. (2017) corresponding to the lowest eigenvalue of a Laplace operator.

Our solutions provide a basic framework in which the effects of anti-VEGF therapy can be understood in terms of biological quantities and parameters. However, these models can be extended and further studied in several ways, as outlined below.

5.2 Future work

There are many ways in which our work can be extended. First, we note that one could replace T with M as the evolving variable in the ODE and PDE models, just as it was in the discrete model.

Though the infinite-extent diffusion problem had a simple solution, the more realistic finite-extent problem had a very complicated separation-of-variables solution that did not converge well near the injection times. However, the main effect of including the diffusion was to *reduce* the dosage and *delay* its maximum (compare the small-time behaviors of Figs. 3 and 13). But these effects can also be more simply modeled by adding decay and delay terms to the concentration. As this just adds a shift to the forcing in the equation for a , such terms should be easy to handle mathematically.

In the paper by Mulyukov et al. (2018), the authors say that their parameters could depend on the initial condition a_0 to some power. This argues for using some sort of nonlinear model for a .

If further work with patient data demonstrates deficiencies with the model, it can be modified to introduce additional degrees of freedom. For instance, a second slope parameter (to be fit) could be added to (25).

As mentioned in the introduction, another way to diagnose the progression of nAMD is to measure the CSFT s . As a first step, one could postulate a linear or logistic growth model for s which is then inhibited by C through the effectiveness factor E . This equation would then replace (2), but the other equations for M and C would remain unaffected.

Acknowledgements The authors would like to thank the reviewers for their helpful comments. The authors would like to thank Novartis (makers of two of the most successful anti-VEGF medicines) for (1) their interest in further developing models from first principles that can guide real world practices and for (2) sharing a small representative sample of BCVA and CSFT data that could guide the thinking expressed in this paper. The work in this manuscript arose out of the 2019 Mathematical Problems in Industry workshop, supported in part by National Science Foundation Grant DMS-1261592. Dr. Kiradjev was partially supported by the EPSRC Centre For Doctoral Training in Industrially Focused Mathematical Modelling (EP/L015803/1).

Appendix

Parameter values from the literature are listed in Table 2, along with dimensionless parameters computed from our definitions. Here the subscripts “A” and “B” refer to two different medications with different dosage recommendations.

The value of k_C was calculated using the quoted value of a half-life of 9 days in Mulyukov et al. (2018). The values of κ were calculated using a time of 28 days between visits. The value of R_1 was calculated as a rough average of the measured

Table 2 Parameter values

Dimensional parameters			Dimensionless parameters	
Parameter	Value	References	Parameter	Value
C_* (mg/mL)	2.1×10^{-3}	Mulyukov et al. (2018)	D_d	487
\tilde{D}_A (mg)	3 or 6		D_A	357 or 714
\tilde{D}_B (mg)	2		D_B	238
\tilde{D} (mm ² /s)	2×10^{-4}	Rattanakijstorn et al. (2018)	\mathcal{D}	1.44
			\mathcal{D}_s	1.44×10^{-3}
k_C (day ⁻¹)	7.70×10^{-2}	Mulyukov et al. (2018)	h	0.15
\tilde{k}_∞ (day ⁻¹)	4.95×10^{-2}	Mulyukov et al. (2018)	k_∞	6.43×10^{-1}
R_e (mm)	12.5	Bekerman et al. (2014)	R_d	1.39
\tilde{R}_i (mm)	4–6	Frenkel et al. (2010)	R_i	0.32
\tilde{R}_1 (mm)	6	Bekerman et al. (2014)	R_1	0.48
\tilde{R}_p (mm)	3.0–3.5	Frenkel et al. (2010)	R_p	0.24
V (mL)	4	Mulyukov et al. (2018)	κ_C	1.16×10^{-1}
			κ_∞	0.25
			$\cos \theta_*$	-0.738

values in Bergmanson and Martinez (2017). The values of R_i and R_j were chosen to maximize R_d . The value of D_d was calculating using the treatment B dosage. The value of V is that for the vitreous fluid, not the entire eyeball.

References

- Awwad S, Lockwood A, Brocchini S, Khaw PT (2015) The PK-Eye: a novel in vitro ocular flow model for use in preclinical drug development. *J Pharm Sci* 104(10):3330–3342. <https://doi.org/10.1002/jps.24480>
- Bekerman I, Gottlieb P, Vaiman M (2014) Variations in eyeball diameters of the healthy adults. *J Ophthalmol* 2014: 5
- Bell W (1968) Special functions for scientists and engineers. Dover books on mathematics. D. Van Nostron, London
- Bergmanson JPG, Martinez JG (2017) Size does matter: what is the corneo-limbal diameter? *Clin Exp Optom* 100(5):522–528
- Blausen.com staff (2014) Medical gallery of Blausen Medical 2014. Wiki J Med. <https://doi.org/10.15347/WJM/2014.010>
- del Amo EM, Rimpelä AK, Heikkinen E, Kari OK, Ramsay E, Lajunen T, Schmitt M, Pelkonen L, Bhattacharya M, Richardson D, Subrizi A, Turunen T, Reinisalo M, Itkonen J, Toropainen E, Casteleijn M, Kidron H, Antopolsky M, Vellonen KS, Ruponen M, Urtti A (2017) Pharmacokinetic aspects of retinal drug delivery. *Prog Retin Eye Res* 57:134–185. <https://doi.org/10.1016/j.preteyeres.2016.12.001>
- Edington M, Connolly J, Chong NV (2017) Pharmacokinetics of intravitreal anti-VEGF drugs in vitrectomized versus non-vitrectomized eyes. *Expert Opin Drug Metab Toxicol* 13(12):1217–1224. <https://doi.org/10.1080/17425255.2017.1404987>
- Falkenstein IA, Cheng L, Freeman WR (2007) Changes of intraocular pressure after intravitreal injection of bevacizumab (avastin). *Retina* 27(8):1044–1047. <https://doi.org/10.1097/IAE.0b013e3180592ba6>
- Frenkel REP, Haji SA, La M, Frenkel MPC, Reyes A (2010) A protocol for the retina surgeon's safe initial intravitreal injections. *Clin Ophthalmol* 4:1279
- Gadkar K, Pastuskovas CV, Le Couter JE, Elliott JM, Zhang J, Lee CV, Sanowar S, Fuh G, Kim HS, Lombana TN, Spiess C, Nakamura M, Hass P, Shatz W, Meng YG, Scheer JM (2015) Design and pharmacokinetic characterization of novel antibody formats for ocular therapeutics. *Investig Ophthalmol Vis Sci* 56(9):5390–5400. <https://doi.org/10.1167/iovs.15-17108>
- Hoyle D, Aslam TM (2017) Generative mathematical modelling to demonstrate virtual simulations of neovascular age related macular degeneration. *PLoS ONE* 12(12):1–12. <https://doi.org/10.1371/journal.pone.0189053>
- Hutton-Smith LA, Gaffney EA, Byrne HM, Maini PK, Schwab D, Mazer NA (2016) A mechanistic model of the intravitreal pharmacokinetics of large molecules and the pharmacodynamic suppression of ocular vascular endothelial growth factor levels by ranibizumab in patients with neovascular age-related macular degeneration. *Mol Pharm* 13(9):2941–2950. <https://doi.org/10.1021/acs.molpharmaceut.5b00849>
- Hutton-Smith LA, Gaffney EA, Byrne HM, Maini PK, Gadkar K, Mazer NA (2017) Ocular pharmacokinetics of therapeutic antibodies given by intravitreal injection: estimation of retinal permeabilities using a 3-compartment semi-mechanistic model. *Mol Pharm* 14(8):2690–2696
- Kotha S, Murtoimäki L (2014) Virtual pharmacokinetic model of human eye. *Math Biosci* 253:11–18. <https://doi.org/10.1016/j.mbs.2014.03.014>
- Martínez-Cañada P, Morillas C, Pino B, Ros E, Pelayo F (2016) A computational framework for realistic retina modeling. *Int J Neural Syst*. <https://doi.org/10.1142/S0129065716500301>
- McHugh KJ, Li D, Wang JC et al. (2019) Computational modeling of retinal hypoxia and photoreceptor degeneration in patients with age-related macular degeneration. *PLoS ONE*. <https://doi.org/10.1371/journal.pone.0216215>
- Mulyukov Z, Weber S, Pigeolet E, Clemens A, Lehr T, Racine A (2018) Neovascular age-related macular degeneration: a visual acuity model of natural disease progression and ranibizumab treatment effect. *CPT Pharmacomet Syst Pharmacol*. <https://doi.org/10.1002/psp4.12322>

- Rattanakisuntorn K, Penkova A, Sadha SS (2018) Mass diffusion coefficient measurement for vitreous humor using FEM and MRI. *IOP Conf Ser Mater Sci Eng* 297:012024. <https://doi.org/10.1088/1757-899x/297/1/012024>
- Roberts PA, Gaffney EA, Luthert PJ, Foss AJE, Byrne HM (2016) Mathematical and computational models of the retina in health, development and disease. *Prog Retin Eye Res* 53:48–69. <https://doi.org/10.1016/j.preteyeres.2016.04.001>
- Schmidt-Erfurth U, Chong V, Loewenstein A, Larsen M, Souied E, Schlingemann R, Eldem B, Monés J, Richard G, Bandello F (2014) Guidelines for the management of neovascular age-related macular degeneration by the European Society of Retina Specialists (EURETINA). *Br J Ophthalmol* 98(9):1144–1167
- Semeraro F, Morescalchi F, Duse S, Gambicorti E, Cancarini A, Costagliola C (2015) Pharmacokinetic and pharmacodynamic properties of anti-VEGF drugs after intravitreal injection. *Curr Drug Metab* 16(7):572–584. <https://doi.org/10.2174/1389200216666151001120831>
- Wykoff CC, Clark WL, Nielsen JS, Brill JV, Greene LS, Heggen CL (2018) Optimizing anti-VEGF treatment outcomes for patients with neovascular age-related macular degeneration. *J Manag Care Spec Pharm* 24(2a Suppl):S3–S15. <https://doi.org/10.18553/jmcp.2018.24.2-a.s3>
- Zhang Y, Bazzazi H, e Silva RL, Pandey NB, Green JJ, Campochiaro PA, Popel AS (2018) Three-dimensional transport model for intravitreal and suprachoroidal drug injection. *Investig Ophthalmol Vis Sci* 59(12):5266–5276

Publisher's Note Springer Nature remains neutral with regard to jurisdictional claims in published maps and institutional affiliations.